ChemComm

COMMUNICATION

View Article Online
View Journal | View Issue

Cite this: *Chem. Commun.*, 2020, **56**, 11879

Received 21st February 2020,
Accepted 24th August 2020

DOI: 10.1039/d0cc01370f

rsc.li/chemcomm

Enhancing the barrier height for Yb(III) single-ion magnets by modulating axial ligand fields†

Aditya Borah, Sourav Dey, Sandeep K. Gupta, Mrinalini G. Walawalkar, Gopalan Rajaraman * and Ramaswamy Murugavel *

The effect of systematic modification of the axial ligand field X on U_{eff} values in Yb(III)-based SIMs, $[Yb(Ph_3PO)_4X_2]X'$ (X, X′ = NO_3 (1), OTf (2) and X = I/Br/Cl; X′ = I_3 (3)), whose equatorial Ph_3PO ligation remains unchanged, has been investigated. Combined magnetic studies coupled with *ab initio* calculations reveal weakening of the axial ligand fields leading to the increase in the energy barrier, apart from suggesting the operation of different relaxation pathways.

The remarkable attention that single-ion magnets (SIMs) have received in recent years is due to their potential applications in high density data storage devices,[1] molecular spintronics[2] and quantum computing devices.[3] Since the discovery of double-decker Tb(III) complex, $[Pc_2Tb][TBA]$,[4] lanthanide-based SIMs have been leading the race to achieve a larger barrier for magnetisation reversal (U_{eff}) and higher blocking temperature (T_B).[5–8] An ideal SIM for potential applications is predicted to be a low-coordinate complex which relaxes *via* the highest excited state, particularly in a linear two-coordinate geometry.[9,10] The tendency of 4f ions, due to their large ionic radii, to form complexes with larger coordination numbers complicates the situation further. However, it has been shown that the combination of strong axial coordination and higher molecular symmetry can result in molecular SIMs that exhibit U_{eff} values even larger than 2000 cm^{-1}.[11,12] Furthermore, complexes with a high-order pseudo axial local symmetry of square antiprismatic,[13] pentagonal bipyramidal,[14–20] hexagonal bipyramidal[21] and sandwich[22–26] have also been found to exhibit excellent SIM properties. Thus, the creation of a compatible, if not ideal, LF environment around lanthanide ions is the key in attaining high values for U_{eff} and T_B in SIMs, through reducing the probability of quantum tunnelling of magnetisation (QTM) and fine tuning the relaxation processes. In this direction, SIMs based on Tb(III), Dy(III) and Er(III) have received a great deal of attention while other 4f ions such as Yb(III) have not been well studied.[27] Other than anisotropy, another important criteria is to stabilise the largest m_J state as the ground state for Yb(III), *viz.* ±7/2; this value is significantly smaller compared to many other Ln(III) ions and hence Yb(III) magnets have not been studied in detail.

Hence, the primary objective of the present study is to systematically weaken the axial ligand field (*e.g.*, varying the Yb-X_{ax} distance) by incorporating different anions at the axial positions while maintaining a higher D_{nh} molecular symmetry. Accordingly, anions NO_3^-, OTf^- and I^- have been chosen to investigate the effect of axial ligand field specifically in prolate Yb(III) mononuclear SIMs. The title Yb(III) complexes $[Yb(Ph_3PO)_4(NO_3)_2][NO_3]\cdot C_2H_5OH$ (**1**), $[Yb(Ph_3PO)_4(OTf)_2][OTf]\cdot(C_2H_5OH)_{0.5}$ (**2**), and $[Yb(Ph_3PO)_4(I_{0.53}Br_{0.47})(I_{0.38}Cl_{0.62})][I_3]\cdot C_2H_5OH$ (**3**) have been synthesized by the reaction of the respective parent hydrated LnX_3 with Ph_3PO in a suitable solvent medium and crystallizing the products under ambient conditions (the bromide and chloride impurities in **3** arise out of HI that was used to prepare YbI_3 from its oxide; details in the ESI†). All three complexes have been characterised by analytical and spectroscopic techniques. Single crystal X-ray diffraction analysis revealed that **1** is an eight-coordinated complex with two chelating nitrates bonded to the Yb(III) centre along with four Ph_3PO ligands while **2** and **3** are six-coordinated complexes comprising four equatorial Ph_3PO ligands along with two axial OTf^- or I^- ligands, respectively (Fig. 1). Continuous shape measurements[28] reveal that the coordination polyhedron of the Yb(III) ion displays D_{2d} symmetry in **1** while it is O_h and D_{4h} in the case of **2** and **3**, respectively (Tables S5 and S6, ESI†). A more significant deviation from O_h in the case of **3** is due to rather long Yb–X bond distances as compared to that of Yb–O(P), resulting in a near D_{4h} geometry around Yb(III). The pseudo-axial Yb–X bonds are significantly longer than the equatorial Yb–O(P) bonds in **1** and **3**. In the case of **2**, the axial and equatorial bond lengths are almost similar, with the average axial bonds being longer only by 0.047 Å. Though there are some significant

Department of Chemistry, Indian Institute of Technology Bombay, Mumbai-400076, India. E-mail: rmv@chem.iitb.ac.in, muruks@iitb.ac.in

† Electronic supplementary information (ESI) available: Synthetic details, crystallographic details, magnetic studies and quantum mechanical calculations. CCDC 1985219–1985221. For ESI and crystallographic data in CIF or other electronic format see DOI: 10.1039/d0cc01370f

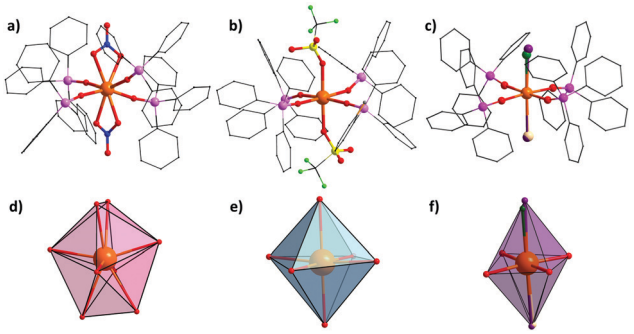

Fig. 1 (a–c) Molecular structures of **1**, **2** and **3**, respectively; (d–f) the respective polyhedral view of the coordination environment of Yb(III). H atoms and lattice anions are omitted for clarity. One part of the disordered coordinated triflate anion is shown for clarity. (Yb, orange; O, red; P, pink; N, blue; S, yellow; F, light green; I, violet; Cl, dark green; Br, tan and C, black).

differences in bond lengths, only the absolute charge on the donor atoms could reflect the strength of axial *vs.* equatorial ligands as we have seen in our earlier examples.[17,21] Due to the presence of twelve phenyl rings of Ph_3PO and one lattice anion X or X′ per molecule, the Yb(III) centres are well separated by 11.7447(2) Å, 11.9967(2) Å and 10.9766(3) Å in **1**, **2** and **3**, respectively, reducing the possibility of long range magnetic interactions between the nearest neighbours (Fig. S4, S6 and S8, ESI†).

The dc magnetic susceptibility measurements show that the room temperature $\chi_m T$ values (2.30, 2.42 and 2.46 $cm^3\ K\ mol^{-1}$ for **1**, **2** and **3**, respectively) are consistent with the expected value for an isolated Yb(III) centre (2.57 $cm^3\ K\ mol^{-1}$; Yb^{III}, $^2F_{7/2}$, $S = 1/2$, $L = 3$, $J = 7/2$, $g_J = 8/7$) (Fig. S11, ESI†). On decreasing the temperature, the $\chi_m T$ values gradually decrease to 1.13, 1.25 and 1.65 $cm^3\ K\ mol^{-1}$ at 2 K for **1**, **2** and **3**, respectively, due to progressive thermal depopulation of the excited Stark sublevels resulting from the spin–orbit coupling and ligand-field effects. The field dependence of magnetization rises slowly at low temperature before reaching 1.74 Nβ (**1**), 1.98 Nβ (**2**), and 1.73 Nβ (**3**) (Fig. S12, ESI†).

To probe the dynamic magnetic behaviour of **1–3**, alternating-current (ac) susceptibility measurements were performed. In the absence of dc field, no out-of-phase signal (χ'') was observed at 1.8 K for all the three complexes due to the presence of high QTM. By applying a suitable dc field, QTM can be partially suppressed/fully quenched. All the ac measurements were carried out in the presence of an optimised field (where the QTM has been suppressed to the highest extent), *i.e.*, 2.5 KOe for **1**, 2 KOe for **2** and 1 KOe for **3** (Fig. S13–S15, ESI†), within a frequency range 0.1–1500 Hz. **1** shows the frequency dependent χ'' peaks in the temperature range 1.8–3.4 K. **2** and **3** possess frequency dependent χ'' peaks up to 6.4 K and 6.95 K, respectively (Fig. 2a–c). This confirms that all three complexes exhibit field induced SIM behaviour, albeit to varying extents. The relaxation times (τ) for **1**, **2** and **3** were determined by fitting the Cole–Cole plots based on the generalised Debye function (Fig. S16–S18 and Tables S7–S9, ESI†). Samples of **1** and **3** relax with a single relaxation process with α values in the range of 0–0.12 and 0–0.23, respectively, indicating a wide distribution of relaxation times. However, the poor fitting of the Cole–Cole plot of **2**, considering it is a single relaxation process, leads us to fit the curves by considering two relaxation processes (fast relaxation (FR) and slow relaxation (SR)) using the modified Debye equation. This affords good agreement between the fit and the experimental data ($0 < \alpha_1 < 0.21$ and $0.01 < \alpha_2 < 0.05$). The linear nature of the plot of $\ln\tau$ *vs.* $1/T$ of **1** reveals that the relaxation occurs *via* an Orbach process (Fig. 2d). The best fit to the Arrhenius equation, $\tau = \tau_0 \exp(U_{eff}/k_B T)$, estimates values of U_{eff} = 9.2 K and $\tau_0 = 1.8 \times 10^{-6}$ s. The non-linear nature of the plot of $\ln\tau$ *vs.* $1/T$ for both **2** and **3** indicates the presence of multiple relaxation pathways, apart from the Orbach process (Fig. 2e and f). The relaxation times have been modeled with QTM, direct, Raman and Orbach processes using the equation: $\tau^{-1} = \tau_{QTM}^{-1} + AT + CT^n + \tau_0^{-1}\exp(-U_{eff}/k_B T)$. In the case of **3**, the best fit to Arrhenius law at a higher temperature estimates U_{eff} = 21.3 K and $\tau_0 = 8.34 \times 10^{-7}$ s. The best fitting of τ using multiple relaxation processes indicates that the relaxation occurs *via* direct and Raman mechanisms ($A = 308.12\ s^{-1}\ K^{-1}$, $C = 11.4\ s^{-1}\ K^{-n}$ and $n = 4.49$). A fitting of τ to the Arrhenius law for **2** at higher temperatures estimates U_{eff} (SR) = 28.2 K, $\tau_0 = 2.88 \times 10^{-8}$ s and U_{eff} (FR) = 27.0 K, $\tau_0 = 3 \times 10^{-7}$ s. The best fitting of τ with multiple relaxation processes indicates the presence of direct and Raman along with Orbach for slow relaxation processes while in the fast relaxation process, the best fit of relaxation time is obtained by considering QTM and Raman together along with Orbach process. (for SR: $C = 0.445\ s^{-1}\ K^{-n}$, $n = 5.53$, $A = 164.45\ s^{-1}\ K^{-1}$ and for FR: $C = 4.02$, $n = 3.58$, $\tau_{QTM} = 0.276$ s). Solid state X-band EPR spectra for **1–3**, recorded at 5 K reveal strong anisotropy in *g*-tensors and partially resolved hyperfine tensors. The *g*-values estimated qualitatively from the spectra are consistent with the earlier reports (Fig. S32, ESI†).[29,30]

To gain further insight into the mechanism of relaxation, *ab initio* CASSCF/RASSI-SO/SINGLE_ANISO calculations have been carried out for complexes **1–3**.[31] Calculation for **1** reveals a large g_{zz} value of 7.0 for the ground Kramers doublet (KD) (Table S11, ESI†). The g_{zz} anisotropy axis is oriented along the NO_3–Yb–NO_3 bond to minimise the electrostatic repulsion (Fig. S19, ESI†) and the four Kramers doublets generated from the $^2F_{7/2}$ state span up to 290.5 cm^{-1} (Table S11, ESI†). The strong transverse anisotropy in the first excited state leads to a large TA-QTM which reinforces the complex to relax *via* the 1st excited KD. While we can tentatively suggest the maximum permissible barrier height for complex **1** as 90.5 cm^{-1}, this is unlikely to be achievable in the experiments as the ground state QTM probabilities are significant, suggesting a significant under barrier relaxation process affirmed by the relatively smaller experimental U_{eff} value of 6.6 cm^{-1} (Fig. 2g). The LoProp charge of the equatorial oxygen atoms becomes larger than the axial oxygen atoms of the nitrate groups revealing a strong equatorial ligand field which is suitable for the Yb(III) ion (Fig. S20 and Table S12, ESI†). The crystal field parameter has been computed using the Stevens formalism $\hat{H}_{CF} = \sum \sum_{k=+q}^{-q} B_k^q O_k^q$ where O_k^q is the extended Stevens operator and B_k^q is the crystal field parameter.[32] The comparable values of axial B_k^q ($k = 0$, $q = 0$) and non-axial B_k^q

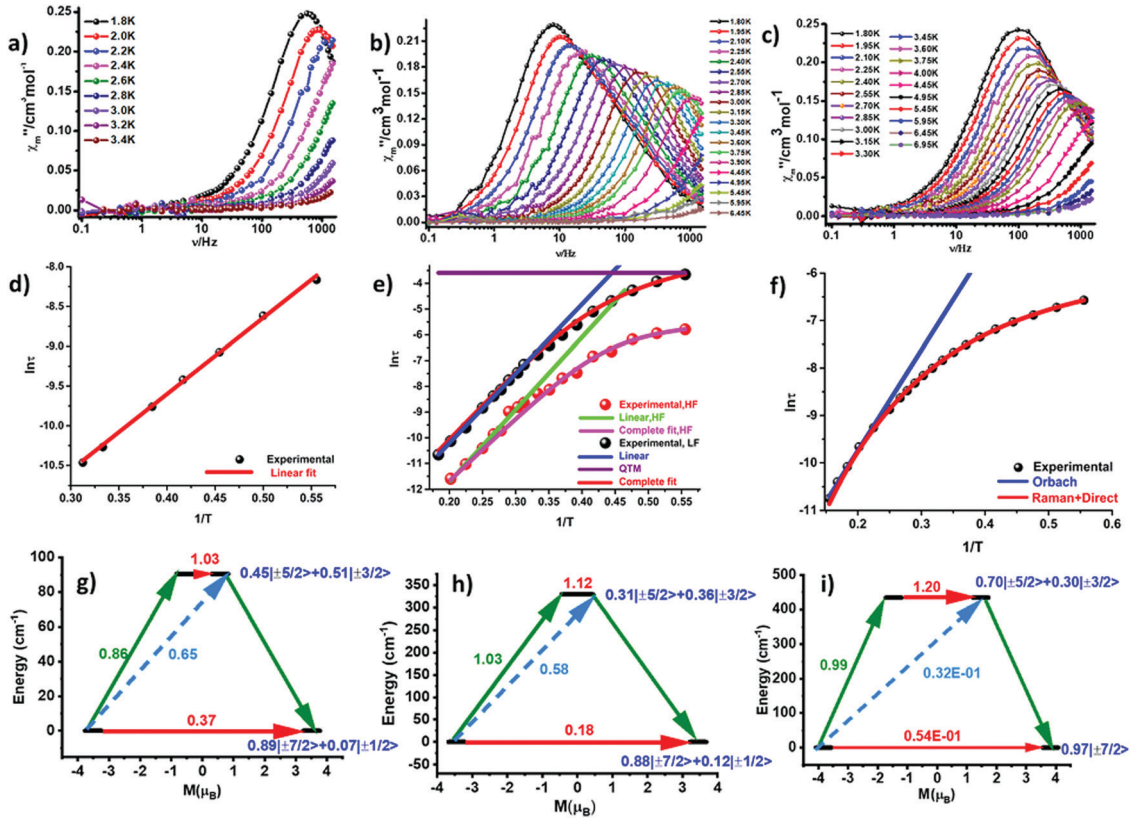

Fig. 2 Frequency dependence of the out-of-phase susceptibilities (χ_M'') for (a) **1**, (b) **2** and (c) **3** under an optimised applied dc field. (d–f) Plot of relaxation time ln τ *vs.* 1/*T* for **1–3**. Blue/green lines represent the best fitting to the Arrhenius law. Red/pink lines represent the best fitting to multiple relaxation processes. *Ab initio* computed mechanism of magnetic relaxation in (g) **1**, (h) **2** and (i) **3I$_2$**. The red line indicates the QTM and TA-QTM *via* ground KD and excited KD, respectively; the olive line indicates the transition probability between KD1 and KD2; and the blue line indicates the Orbach relaxation mechanism. The blue characters indicate the m_J composition of each KD.

($k \neq 0$, $q = 2, 4$) parameters imply significant QTM which is reflected in the relaxation mechanism (Table S13, ESI† and Fig. 2).

The replacement of NO_3 groups in **1** by OTf groups in **2** (or iodide/bromide/chloride ion in complex **3**) results in the decrease of transverse anisotropy (weakening of the axial ligand field in **2** and **3**) and this is reflected in a smaller QTM at the ground state compared to **1** in the relaxation pathways with complex **3** (with the iodide in both axial position) possessing the least (Tables S14–S18, Fig. 2h and i, see Fig. S22 for anisotropy axis, ESI†). The axial position of **3** is found to be a superposition of iodide along with Cl^- and Br^- ion impurities. In this regard, we have performed additional calculations on the crystal structure of **3** considering two I^- (model **3I$_2$**); one I^- and Br^- (model **3IBr**); one I^- and Cl^- (model **3ICl**); and one Br^- and Cl^- (model **3BrCl**) in the axial position. The CASSCF/RASSI-SO/SINGLE-ANISO calculation reveals the increase of energy splitting of four KDs in the order **3BrCl** < **3ICl** < **3IBr** < **3I$_2$** (Tables S15–S18, ESI†). This order is correlated to the decrease in the LoProp charge of the axial atoms from **3BrCl** to **3I$_2$**, which stabilises the prolate electron density of Yb (Table S20 and Fig. S24, ESI†).

The energy gap between the ground and first excited KD is 329.3 cm^{-1} for **2** (386.5 cm^{-1} for **3**), which is three times larger than that obtained for **1** (Tables S14–S18, ESI†). The energy gap between the ground and first excited KD of **3** was estimated from weightage of the partial occupancy of I, Br and Cl (0.23 (**3I$_2$**)+ 0.21 (**3IBr**) + 0.29 (**3ICl**) + 0.27 (**3BrCl**)) in **3**. Similar to complex **1**, the maximum permissible barrier could only be estimated and this is found to be 329.3 cm^{-1} and 386.5 cm^{-1} for complexes **2** and **3**, respectively. Experimentally, the U_{eff} was estimated with the presence of an applied field and this is found to be slightly larger for **2** compared to **3**. However, as different optimised dc fields are applied for these sets, this makes the comparison to the estimated maximum permissible barrier cumbersome. This leads to a larger U_{eff} for **2** compared to **3**, in contrast to the U_{cal} value. As the QTM probabilities are still high for both **2** and **3**, clearly here as well under-barrier relaxations are expected to dominate as revealed by the smaller experimental U_{eff} values. In **3**, the LoProp charge of the axial atoms (I/Br/Cl) is the lowest compared to **1** and **2** suggesting an improvement in the SIM behaviour as witnessed in the experiments. It is also important to note that this B_2^0 parameter becomes the largest for **3** (**3I$_2$**) compared to both **1** and **2** (Table S13, ESI†). We have also plotted the β-electron density of Yb(III) as shown in earlier examples of Dy(III)[33] and here the electron density shape is found to be prolate which implies that a strong equatorial ligand field is present in all the complexes (Fig. S28, ESI†).

In principle, the largest barrier heights can be achieved for these complexes by removing the axial ligands. Since the equatorial

ligands are the same in **1–3,** additional *ab initio* calculations were performed on model **3a** (**3I$_2$**) where the axial iodide was removed from **3** (Fig. S29 for anisotropy axis, ESI†). Calculations reveal large splitting of KDs (1984.4 cm^{-1}) along with a very small QTM ($0.01\mu_B$) probability (Table S24 and Fig. S30, ESI†). The model complex relaxes *via* the 1st excited KD due to large transverse anisotropy which results in the U_{cal} value of 1081 cm^{-1}. The axial crystal field parameter becomes very large compared to complexes **1–3** (Table S13, ESI†), implying that record barrier heights are achievable in Yb(III) SIMs if a suitable ligand environment is offered.

To assess the role of axial ligands in **1–3**, models **1b**, **2b** and **3b** (**3I$_2$**) are constructed wherein the equatorial ligands have been removed. The calculations reveal strong transverse anisotropy in the ground KD resulting in large QTM in the ground state as expected for such strongly prolate Yb(III) ions (Tables S25–S27, ESI†). The anisotropy becomes negligible at the fourth KD. The absence of the equatorial ligand stabilises a lower m_J level as the ground state resulting in the oblate nature of the electron density in the models **1b–3b** (Fig. S28, ESI†), underlining the importance of a strong equatorial ligand field to realise stable zero-field Yb SIMs. Furthermore, a linear correlation has been found for the KD2–KD1 energy gap with axial crystal field parameter B_2^0 and the average Loprop charge of the axial atoms coordinated to Yb(III) and of complexes **1**, **2** and **3** (**3I$_2$**) (see Fig. S31, ESI†). The computed energy gap is found to be inversely proportional to the average axial LoProp charge and proportional to B_2^0. This correlation reveals that a very small axial crystal field which will lead to large B_2^0 value is all that is needed to achieve improved SIM behaviour in Yb(III) complexes.

In conclusion, this study presents a careful effort to fine-tune the axial CF to enhance the magnetic reversal barrier heights. To the best of our knowledge, **2** and **3** exhibit field-induced SIM behaviour with the highest observed barrier heights among all hexacoordinated mononuclear Yb(III)-based SIMs so far reported. Further weakening of the axial field is likely to result in even more improved Yb(III) SIMs.

This work was supported by SERB (EMR/2017/002767 and SB/S2/JCB-85/2014 to RM and CRG/2018/000430 to GR) and DST ((DST/SJF/CAS-03/2018-19 to GR and SR/WOS-A/CS-15/2017 to MGW). AB and SD thank UGC for fellowships. We acknowledge Dr D. Aravena for providing the code to plot beta electron density and Prof. J. J. Vittal for helping us out with resolving a disorder. We thank the reviewers for their useful suggestions.

Conflicts of interest

There are no conflicts to declare.

References

1 M. Mannini, F. Pineider, P. Sainctavit, C. Danieli, E. Otero, C. Sciancalepore, A. M. Talarico, M.-A. Arrio, A. Cornia, D. Gatteschi and R. Sessoli, *Nat. Mater.*, 2009, **8**, 194–197.
2 R. Vincent, S. Klyatskaya, M. Ruben, W. Wernsdorfer and F. Balestro, *Nature*, 2012, **488**, 357–360.
3 P. C. Stamp and A. Gaita-Arino, *J. Mater. Chem.*, 2009, **19**, 1718–1730.
4 N. Ishikawa, M. Sugita, T. Ishikawa, S.-Y. Koshihara and Y. Kaizu, *J. Am. Chem. Soc.*, 2003, **125**, 8694–8695.
5 L. Sorace, C. Benelli and D. Gatteschi, *Chem. Soc. Rev.*, 2011, **40**, 3092–3104.
6 D. N. Woodruff, R. E. Winpenny and R. A. Layfield, *Chem. Rev.*, 2013, **113**, 5110–5148.
7 S. K. Gupta and R. Murugavel, *Chem. Commun.*, 2018, **54**, 3685–3696.
8 J. D. Rinehart and J. R. Long, *Chem. Sci.*, 2011, **2**, 2078–2085.
9 L. Ungur and L. F. Chibotaru, *Phys. Chem. Chem. Phys.*, 2011, **13**, 20086–20090.
10 N. F. Chilton, *Inorg. Chem.*, 2015, **54**, 2097–2099.
11 F.-S. Guo, B. M. Day, Y.-C. Chen, M.-L. Tong, A. Mansikkamäki and R. A. Layfield, *Science*, 2018, **362**, 1400–1403.
12 P. Evans, D. Reta, G. F. Whitehead, N. F. Chilton and D. P. Mills, *J. Am. Chem. Soc.*, 2019, **141**, 19935–19940.
13 W. Cao, C. Gao, Y.-Q. Zhang, D. Qi, T. Liu, K. Wang, C. Duan, S. Gao and J. Jiang, *Chem. Sci.*, 2015, **6**, 5947–5954.
14 Y.-C. Chen, J.-L. Liu, L. Ungur, J. Liu, Q.-W. Li, L.-F. Wang, Z.-P. Ni, L. F. Chibotaru, X.-M. Chen and M.-L. Tong, *J. Am. Chem. Soc.*, 2016, **138**, 2829–2837.
15 Y. S. Ding, N. F. Chilton, R. E. Winpenny and Y. Z. Zheng, *Angew. Chem., Int. Ed.*, 2016, **55**, 16071–16074.
16 S. K. Gupta, T. Rajeshkumar, G. Rajaraman and R. Murugavel, *Chem. Commun.*, 2016, **52**, 7168–7171.
17 S. K. Gupta, T. Rajeshkumar, G. Rajaraman and R. Murugavel, *Chem. Sci.*, 2016, **7**, 5181–5191.
18 S. K. Gupta, T. Rajeshkumar, G. Rajaraman and R. Murugavel, *Dalton Trans.*, 2018, **47**, 357–366.
19 M. S. Norre, C. Gao, S. Dey, S. K. Gupta, A. Borah, R. Murugavel, G. Rajaraman and J. Overgaard, *Inorg. Chem.*, 2020, **59**, 717–729.
20 S. Dey and G. Rajaraman, *J. Chem. Sci.*, 2019, **131**, 124.
21 A. B. Canaj, S. Dey, E. R. Martí, C. Wilson, G. Rajaraman and M. Murrie, *Angew. Chem.*, 2019, **131**, 14284–14289.
22 K. R. Meihaus and J. R. Long, *J. Am. Chem. Soc.*, 2013, **135**, 17952–17957.
23 K. R. McClain, C. A. Gould, K. Chakarawet, S. J. Teat, T. J. Groshens, J. R. Long and B. G. Harvey, *Chem. Sci.*, 2018, **9**, 8492–8503.
24 C. A. Gould, K. R. McClain, J. M. Yu, T. J. Groshens, F. Furche, B. G. Harvey and J. R. Long, *J. Am. Chem. Soc.*, 2019, **141**, 12967–12973.
25 M. J. Giansiracusa, A. K. Kostopoulos, D. Collison, R. E. Winpenny and N. F. Chilton, *Chem. Commun.*, 2019, **55**, 7025–7028.
26 R. Collins, M. J. Heras Ojea, A. Mansikkamäki, J. Tang and R. A. Layfield, *Inorg. Chem.*, 2020, **59**, 642–647.
27 F. Pointillart, O. Cador, B. Le Guennic and L. Ouahab, *Coord. Chem. Rev.*, 2017, **346**, 150–175.
28 M. Llunell, D. Casanova, J. Cirera, J. Bofill, P. Alemany and S. Alvarez, *SHAPE (Version 2.1)*, Barcelona, 2013.
29 K. S. Pedersen, A.-M. Ariciu, S. McAdams, H. Weihe, J. Bendix, F. Tuna and S. Piligkos, *J. Am. Chem. Soc.*, 2016, **138**, 5801–5804.
30 K. S. Pedersen, J. Dreiser, H. Weihe, R. Sibille, H. V. Johannesen, M. A. Sørensen, B. E. Nielsen, M. Sigrist, H. Mutka and S. Rols, *Inorg. Chem.*, 2015, **54**, 7600–7606.
31 F. Aquilante, J. Autschbach, R. K. Carlson, L. F. Chibotaru, M. G. Delcey, L. De Vico, I. Fdez. Galván, N. Ferré, L. M. Frutos, L. Gagliardi, M. Garavelli, A. Giussani, C. E. Hoyer, G. Li Manni, H. Lischka, D. Ma, P. Å. Malmqvist, T. Müller, A. Nenov, M. Olivucci, T. B. Pedersen, D. Peng, F. Plasser, B. Pritchard, M. Reiher, I. Rivalta, I. Schapiro, J. Segarra-Martí, M. Stenrup, D. G. Truhlar, L. Ungur, A. Valentini, S. Vancoillie, V. Veryazov, V. P. Vysotskiy, O. Weingart, F. Zapata and R. Lindh, *J. Comput. Chem.*, 2016, **37**, 506–541.
32 L. F. Chibotaru and L. Ungur, *J. Chem. Phys.*, 2012, **137**, 064112.
33 D. Aravena and E. Ruiz, *Inorg. Chem.*, 2013, **52**, 13770–13778.

